Title

Development of a patient-specific two-compartment anthropomorphic breast phantom

Journal

Physics in Medicine and Biology, 57(13)

ISSN

0031-9155

Authors

Prionas, Nicolas D

Burkett, George W

McKenney, Sarah E

et al.

Publication Date

2012-07-07

DOI

10.1088/0031-9155/57/13/4293

Peer reviewed

Published in final edited form as:
Phys Med Biol. 2012 July 7; 57(13): 4293–4307. doi:10.1088/0031-9155/57/13/4293.

Development of a Patient-Specific Two-Compartment Anthropomorphic Breast Phantom

Nicolas D. Prionas, Ph.D.[1], **George W. Burkett, M.S.**[1], **Sarah E. McKenney, B.S.**[1], **Lin Chen, M.S.**[1], **Robin L. Stern, Ph.D.**[2], and **John M. Boone, Ph.D.**[1]

John M. Boone: jmboone@ucdavis.edu

[1]University of California Davis Medical Center, Department of Radiology, 4860 Y Street, Suite 3100, Sacramento, CA 95817, USA, 916-734-2497 (tel) 916-734-6548 (fx)

[2]University of California Davis Medical Center, Department of Radiation Oncology Sacramento, CA 95817, USA

Abstract

Purpose—To develop a technique for the construction of a two-compartment anthropomorphic breast phantom specific to an individual patient's pendant breast anatomy.

Methods—Three-dimensional breast images were acquired on a prototype dedicated breast computed tomography (bCT) scanner as part of an ongoing IRB-approved clinical trial of bCT. The images from the breast of a patient were segmented into adipose and glandular tissue regions and divided into 1.59 mm thick breast sections to correspond to the thickness of polyethylene stock. A computer controlled water-jet cutting machine was used to cut the outer breast edge and the internal regions corresponding to glandular tissue from the polyethylene. The stack of polyethylene breast segments was encased in a thermoplastic "skin" and filled with water. Water-filled spaces modeled glandular tissue structures and the surrounding polyethylene modeled the adipose tissue compartment. Utility of the phantom was demonstrated by inserting 200 μm microcalcifications as well as measuring point dose deposition during bCT scanning.

Results—Rigid registration of the original patient images with bCT images of the phantom showed similar tissue distribution. Linear profiles through the registered images demonstrated a mean coefficient of determination (r^2) between grayscale profiles of 0.881. The exponent of the power law describing the anatomical noise power spectrum was identical in the coronal images of the patient's breast and the phantom. Microcalcifications were visualized in the phantom at bCT scanning. Real-time air kerma rate was measured during bCT scanning and fluctuated with breast anatomy. On average, point dose deposition was 7.1% greater than mean glandular dose.

Conclusions—A technique to generate a two-compartment anthropomorphic breast phantom from bCT images has been demonstrated. The phantom is the first, to our knowledge, to accurately model the uncompressed pendant breast and the glandular tissue distribution for a specific patient. The modular design of the phantom allows for studies of a single breast segment and the entire breast volume. Insertion of other devices, materials, and tissues of interest into the phantom provide a robust platform for future breast imaging and dosimetry studies.

Keywords

Computed tomography; breast; phantom

1. Introduction

Early detection of breast cancer and the early initiation of curative treatment are critical in improving patient outcomes (Joensuu *et al.*, 2004; Shen *et al.*, 2005). As a result, there has

been a broad push toward the development of new imaging technologies that allow for earlier lesion detection. Mammography is currently the gold standard imaging modality for breast cancer screening; however, tomographic imaging modalities, such as dynamic contrast-enhanced magnetic resonance imaging (DCE-MRI), dedicated breast cone-beam computed tomography (bCT), and digital breast tomosynthesis (DBT) are being investigated as modalities to improve lesion visualization.

In developing a new imaging technology, technical evaluation for system optimization is essential before the modality can be used for clinical evaluation. Phantoms play an important role in this research and development process. Medical imaging phantoms can be categorized as computational or physical. Computational breast phantoms benefit from great flexibility; they can be generalized to represent the statistical variability in a population (Huang *et al.*, 2011; Bakic *et al.*, 2011) or can be designed to accurately model the anatomy of a single individual (Li *et al.*, 2009). Using the elemental breast tissue compositions published by Hammerstein (1979), computational phantoms can accurately describe tissue properties in a voxelized nature for Monte Carlo simulations (Darambara *et al.*, 2009). Computational breast phantoms are particularly useful for imaging system technique optimization before prototype development (Chen *et al.*, 2011). Furthermore, image quality can be optimized with respect to simulations of patient dose.

Physical phantoms complement computational phantoms, providing a method for experimental measurement and validation. Ultimately, physical phantoms allow for a ground-truth characterization of the actual performance of an imaging system. Physical phantoms are important in image system characterization and optimization. Specifically in the case of bCT, physical phantoms are used to characterize a system's response to x-ray scatter from an object (Cai *et al.*, 2011). They are also used in optimizing specific imaging tasks, such as microcalcification detection (Lai *et al.*, 2007). Since all imaging with ionizing radiation must be performed in the context of a reasonable dose to the patient, physical phantoms are also useful in dosimetry. Similarly, physical phantoms are used to study higher energy x-ray procedures, such as those for breast radiation therapy (Almberg *et al.*, 2011).

The variety of physical phantoms previously used to represent the breast is extensive and ranges from basic geometries to highly complex anthropomorphic phantoms. In the simplest case, polyethylene cylinders have been used to approximate the breast for studies of x-ray scatter (Yang *et al.*, 2008). More recently, phantoms of a compressed breast have been constructed based on computational models (Carton *et al.*, 2011). However, most physical phantoms currently model the compressed breast for use in studies of mammography and DBT (Caldwell and Yaffe, 1990; Freed *et al.*, 2011a). While these models simulate breast architecture and anatomical noise, they are based on projection images through the compressed breast and do not accurately reflect the volumetric distribution of glandular and adipose tissues. There is a need for an accurate physical phantom of the uncompressed breast in a pendant position to allow for phantom studies of modalities employing this geometry, such as dedicated breast CT and prone breast radiotherapy.

The purpose of this work was to develop a technique for the construction of a two-compartment anthropomorphic breast phantom specific to an individual patient's pendant breast anatomy.

2. Materials and Methods

2.1. Patient Imaging

Patient images were acquired on a previously-described prototype dedicated breast computed tomography scanner (Lindfors *et al.*, 2008; Prionas *et al.*, 2011) as a part of an

ongoing Institutional Review Board approved clinical trial of bCT. Women with mammographically identified Breast Imaging Reporting and Data System (BI-RADS) category 4 or 5 lesions were recruited for bCT imaging. Patients were scanned prone, imaging one breast at a time, without compression, and in pendant geometry. Breast CT technique factors were set to a tube potential of 80 kVp (filtered by 0.2 mm copper) and tube current selected such that the mean glandular dose (MGD) was equivalent to that of two-view screening mammography. Images were acquired by means of a 40 cm by 30 cm indirect flat panel detector (Varian Medical Systems, Palo Alto, CA) with 2 by 2 pixel binning to achieve an effective pixel pitch of 388 μm. Images were reconstructed using a cone-beam filtered backprojection reconstruction algorithm and a 512 by 512 matrix to achieve an in-plane pixel pitch of approximately 208 μm and slice thickness on the order of 200 μm.

The breast image chosen for phantom development was selected to represent an average breast diameter and glandularity (Huang *et al.*, 2011). The patient was a 59-year-old woman diagnosed with a benign cyst (Figure 1a).

2.2. Image Processing

The breast volume data set was segmented using a previously described segmentation algorithm (Packard and Boone, 2007; Yaffe *et al.*, 2009) which employs median filtering, histogram-based iterative thresholding, and a connected-components algorithm to delineate air, fibroglandular tissue, adipose tissue, chest wall muscle, and skin. The segmented data set was simplified to three compartments (air, adipose tissue, and glandular tissue) by removing the skin (replaced with air) and defining the chest wall and fibroglandular tissue as a single soft-tissue compartment (Figure 1b).

The segmented data set was then median filtered and two-step morphological opening (two erosions followed by two dilations) was used to remove single pixel protrusions at all edges. The median voxel value in 1.59 mm thick sections of tissue was used to generate a new volume data set with slice thickness equal to the stock polyethylene; slice thickness, instead of slice-to slice separation, was used to define the distance between image segments. Any bodies of adipose tissue surrounded by glandular tissue were eliminated from the model as they would result in free floating polyethylene pieces in the final phantom.

Edge detection was performed to identify the adipose tissue edge surrounding the circumference of the breast and the edges of all the glandular tissue structures within the breast. Connected components were identified in the adipose and glandular edges using a minimum threshold of 50 and 30 elements, respectively, in order to eliminate outlines that were below the resolution of the water-jet cutting instrument. For each detected edge, the coordinates of all the elements were recorded in sequential order using a radial sweep algorithm to trace along the outline.

Each list of edge coordinates was post-processed before entry into computer-aided design (CAD) software to ensure that each list formed a single closed loop with a common start and stop point. Redundant data points were eliminated to allow for accurate B-spline fitting of each edge. In the case of redundant data points separated by one point between them, all three points were removed. For two closed loops connected by a single voxel-wide septum, the redundant points in the septum were expanded to two parallel lines, transforming the two closed loops into one. The model was simplified by reducing the number of points defining a given edge. Multiple points in a horizontal, vertical, or diagonal line (represented by stair-stepping pixels with a slope of plus or minus one) were reduced to include only the first and last point (Figure 2).

2.3. Computer-aided Design Model Development

The adipose tissue and glandular tissue edge coordinates were used to generate a CAD model consisting of 1.59 mm polyethylene segments (Figure 1c) stacked sequentially from chest wall to nipple to recreate the breast volume (Figure 3a,b). The model was created using SolidWorks 2009 SP3.0 (Dassault Systèmes SolidWorks Corp., Concord, MA). Each edge coordinate list was fit using a B-spline to create a smooth outline. The adipose edge was used to extrude a 1.59 mm thick representation of a breast segment. The glandular tissue edges were then used to cut out regions from the breast segment corresponding to islands of glandular tissue.

Each segment in the solid model was visually inspected to ensure the accuracy of tissue structure delineation and subsequently manipulated to insert artificial features for orientation. Two locating notches were cut out of the circumference of each breast segment at 90 degrees from each other. Corresponding alignment tools were designed to fit into the locating notches to help align the breast segments during phantom assembly. The shapes of the alignment tools match the anterior-posterior contour of the breast along perpendicular planes through the breast.

2.4. Phantom Construction and Assembly

The individual breast segments were exported in a “*.dxf” format compatible with computer numerical controlled (CNC) machining software. The stack of breast segments was machined from 1.59 mm thick ultrahigh molecular weight polyethylene sheets using a 0.2 mm wide water-jet with the tool path centerline defined at the tissue structure edges. The machined breast segments were stacked on top of each other, beginning with the largest posterior segment and ending with the smallest segment near the nipple, and aligned using the two perpendicular alignment tools (Figure 3c).

An outer container was molded around the breast phantom using 1.6 mm thermoplastic (WFR-Aquaplast/Qfix Systems Avondale, PA) to approximate the thickness of breast skin (Huang *et al.*, 2008). The container holding the stack of breast segments was filled with water such that the air gaps in the phantom, representing the glandular tissue compartment, were filled with water.

2.5. Breast Tissue Distribution Accuracy

The complete breast phantom, filled with water, was scanned on the prototype bCT scanner using 80 kVp and 4.5 mA. The resulting images were registered to the original patient images using RView version 9 (Studholme, 2010). Line profiles through four representative segments of the registered and overlaid phantom and original breast images were evaluated to compare the tissue distributions.

Breast tissue distribution was also evaluated using the anatomical noise power spectrum. The noise power spectrum was measured in the unregistered volume data sets of the patient’s breast and the phantom and the exponent of the power law (β) was used to characterize anatomical noise, as has been previously described (Chen *et al.*, 2012; Metheany *et al.*, 2008; Burgess *et al.*, 2001). Anatomical noise was characterized in three orthogonal planes of each volume data set and compared.

Mean Hounsfield unit (HU) values of the phantom materials (polyethylene, water, thermoplastic, and paraffin wax) and native breast tissues (adipose, glandular, and skin) were measured from three independent regions of interest within each tissue in each image set. The HU values of breast tissues and their surrogate phantom materials were compared

using Student's t test. Adipose tissue was compared to polyethylene and paraffin wax, glandular tissue was compared to water, and skin was compared to thermoplastic.

2.6. Microcalcification Insertion

Microcalcifications were inserted into the phantom in one of the breast segments. The segment is 7.0 cm from the chest wall of the phantom (~61% of phantom length) and has a diameter of 7.5 cm. Paraffin wax was packed into three distinct regions of the segment. Approximately five calcium carbonate particles (CIRS Inc., Norfolk, VA) measuring 200–212 μm in size were embedded within the wax. A digital mammogram projection image of the segment containing the microcalcifications was acquired at 25 kVp and 80 mA using a rhodium filter. The mammographic projection served as a ground-truth image of the actual location of the microcalcifications. The entire breast phantom with the microcalcifications was scanned on a prototype bCT scanner in a prone orientation, using 80 kVp and 4.5 mA (75 mAs).

2.7. bCT Dose Assessment

Mean glandular dose (MGD) was estimated and compared to point dose measurements made in the glandular compartment of the phantom. Measurements were performed over a range of x-ray tube potentials and tube currents (Table 1). The maximum tube current was selected for each tube potential; however, the technique used to acquire the original patient images (80 kVp and 4.5 mA) was also evaluated to represent a more realistic dose from bCT.

Mean glandular dose (D_g) was calculated as the product of the polyenergetic normalized glandular dose coefficient used in bCT (D_gN_{CT}) and exposure measured in air at isocenter (X_{Iso}).

$$D_g = D_g N_{CT} \times X_{Iso} \tag{1}$$

A thimble real-time air ionization chamber that is also capable of conventional integrated measurements was used to measure exposure (RadCal Corporation, Monrovia, CA). The polyenergetic D_gN_{CT} coefficients were computed as

$$D_g N_{CT} = \frac{\int_0^{E_{\max}} \Phi_{(E)F(E)dE}}{\int_0^{E_{\max}} \Phi_{(E)K(E)dE}} \tag{2}$$

for a photon fluence Φ(E) in photons/mm^2, Monte Carlo derived glandular dose per fluence F(E) in μGy/(10^6 photons/mm^2), and air kerma per fluence K(E) in μGy/(10^6 photons/mm^2). The photon fluence, Φ(E), for each tube potential was derived using tungsten anode spectral model interpolating polynomials (TASMIP) assuming a 0.15% x-ray generator ripple and modified to match half-value layer (HVL) measurements performed on the prototype bCT scanner. The glandular dose per fluence, F(E), was generated using the previously validated SIERRA Monte Carlo code system. The air kerma per fluence, K(E), was calculated as the product of energy fluence and mass energy transfer coefficient.

Exposure measurements were made in the phantom during complete bCT scans with the real-time dosimeter placed in the glandular tissue compartment at the mid-breast level (Figure 4). Exposure measured within the phantom was converted to dose using the polyenergetic f-factor for glandular tissue, which was calculated as a spectrally weighted

average from monoenergetic mass energy absorption coefficients for glandular tissue and air (Figure 5).

3. Results

The patient's breast measured approximately 8.9 cm in length and 14.3 cm in diameter as measured at the chest wall. It had a total volume of 579.7 cm^3 and a volume glandular fraction of 22.1%. The breast phantom measured 11.5 cm in length and approximately 13.9 cm in diameter at its base. The total volume was 804.5 cm^3 and the volume glandular fraction was measured to be 17.0%.

Affine registration, with contraction in the anterior-posterior direction, demonstrated in-plane similarity between the original patient images and bCT images of the breast phantom (Figure 6). The phantom lacked some fine glandular tissue structures, but larger bodies of glandular tissue closely matched the original patient images. The thermoplastic "skin" demonstrated an inhomogeneous thickness and was generally thicker than the patient's skin. Line profiles through four segments of the registered patient and phantom images showed similar grayscale profiles with an average coefficient of determination (r^2) of 0.881 ± 0.044 (standard deviation). Anatomical noise in the coronal plane, as described by β, was 2.55 in both the patient's breast and the phantom. The value of β for the patient's breast and the phantom, respectively, were 2.44 and 2.02 in the axial plane and 2.51 and 1.96 in the sagittal plane.

The polyethylene, water, thermoplastic, and paraffin wax used to construct the phantom had mean (± standard deviation) HU values of −214 ± 10, −73 ± 13, −88 ± 42, and −212 ± 34 HU, respectively. The native breast tissues (adipose, glandular, and skin) measured −220 ± 9, −87 ± 16, and −95 ± 9 HU. The differences between breast tissues and their phantom surrogates were not statistically significant.

Insertion of microcalcifications into the phantom demonstrated the potential application of the phantom for microcalcification visualization studies. At mammography, 6 microcalcifications were detected in the cluster at the 11 o'clock position, 7 in the 2 o'clock cluster, and 6 in the 4 o'clock cluster (Figure 7). In coronal bCT images, 0% (0/6), 71.4% (5/7), and 66.6% (4/6) of microcalcifications were visualized at the 11, 2, and 4 o'clock positions, respectively, for a mean detection rate of 46%. Microcalcification detection in the axial and sagittal planes was difficult. Orthogonal CT images containing the microcalcification cluster at the 4 o'clock position are shown in Figure 7.

A 0.6 cm^3 thimble real-time air ionization chamber was introduced into the glandular tissue compartment of the phantom. The phantom measured approximately 9 cm in diameter at the level of the measurements. During bCT scanning, the first projection image was acquired with the x-ray tube at approximately 42°, where 0° was defined at the superior aspect of the breast and positive angles were measured in the direction of x-ray tube motion (clockwise). Air kerma rate decreased as the x-ray tube rotated around the phantom, reaching a minimum when the source was farthest from the dosimeter (approximately 230°). A drop in the real-time air kerma rate at approximately 143° matched closely to when a majority of the beam passed through the longest dimension of water (Figure 8). On average, across the seven sets of technique factors evaluated, the point dose measured using the real-time dosimeter was 7.1 ± 0.6% greater than computed MGD (Table 1).

4. Discussion and Conclusions

A technique to generate a two-compartment anthropomorphic breast phantom from the three-dimensional bCT image set of a specific patient was demonstrated. Previous studies

have developed uncompressed breast phantoms with a stochastic glandular tissue distribution approximating patient data (Freed *et al.*, 2011b; Cai *et al.*, 2011). The physical phantom generated in our study is the first non-cadaveric and non-tissue-based phantom, to our knowledge, to accurately model the uncompressed breast and the glandular tissue distribution for a specific patient.

In-house software was generated to automate large portions of the phantom design technique allowing for rapid, low-cost construction of a 3D breast phantom. However, it should be noted that the visual inspection of model accuracy and model assembly can be time consuming steps in the design process, depending on the level of accuracy that is desired. Further software automation to compare the breast segment CT images with corresponding CAD model images may expedite this quality assurance process.

The two compartments of the phantom, representing adipose tissue and glandular tissue, were constructed from polyethylene and water, respectively, based on the similarity in linear attenuation coefficients. The linear attenuation coefficients of adipose tissue and polyethylene, for x-ray spectra used in bCT imaging, have been previously shown to be within 2% of each other; glandular tissue and water have linear attenuation coefficients within 3% of each other (Prionas *et al.*, 2011). Similarly, paraffin wax has comparable attenuation coefficient and density as adipose tissue and has been used as a phantom material by other groups (Shen *et al.*, 2011). At higher x-ray energies, such as those used in radiotherapy, the differences in linear attenuation are expected to be even smaller. Thermoplastic was used as a skin-like container for the phantom due to its malleability to form a continuous enclosure around the phantom and its established use as a tissue-equivalent bolus material. Ultimately, the materials used for phantom construction showed no statistically significant difference in HU value from their native tissue equivalents.

The phantom was designed to be modular such that studies can be performed on the entire breast volume or on a single breast segment. The modular design of the phantom allows for the insertion of other objects into any point in the glandular tissue compartment. In this study, we demonstrated the insertion of microcalcifications embedded in paraffin wax, but other inserts could include vials of iodinated contrast medium, gold nanoparticles, malignant or benign tissue specimens, radioactive sources, and various dosimeters.

The potential for breast dosimetry using the phantom was demonstrated by measuring real-time dose deposition in the breast during bCT scanning. A 0.6 cm^3 thimble air ionization chamber was used to measure point dose, but thermoluminescent or MOSFET dosimeters could be used to measure dose at multiple locations simultaneously. The mid-breast point dose measured using the air ionization chamber was ~7% greater than the MGD computed using more conventional methods. This is likely due to the off-center position of the measurement. With more measurements throughout the glandular tissue compartment using smaller dosimeters, MGD could be compared to a true average of point dose measurements in order to evaluate the accuracy of D_gN_{CT} coefficients.

The anthropomorphic phantom has several potential applications. As a generic breast phantom, it can be used to evaluate image quality, to optimize imaging system technique factors, and to study lesion detection. The phantom may be used in a variety of visualization studies and serve as an adjunct to observer studies, but computational phantoms will always play an important role in observer studies requiring a large number of images. The patient-specific design of the phantom allows for studies which consider the anatomy and tissue distribution for an individual patient, as demonstrated through real-time dosimetric assessment. Dosimetry in the phantom may also be useful during simulated treatment of the

pendant breast during external beam radiation therapy or during brachytherapy with an implanted radioactive source.

The design and construction of this phantom had several limitations. While the phantom is intended to exactly model the breast anatomy of a given patient, there are inherent errors in the manufacturing and assembly processes that make this challenging. The error tolerance in material thickness and gaps between breast segments resulted in a phantom that was 2.6 cm longer than the patient's breast. During image processing, CT slice thickness, instead of slice-to-slice separation, was used to calculate distance in the posterior-anterior direction, resulting in a 1.8 mm increase in the length of the phantom. At phantom assembly, water was trapped between breast segments, resulting in added length. In the fully assembled phantom, compression of the breast segments minimized the water gaps (Figure 7); however with less compression and with the phantom positioned askew form the coronal plane, the water gaps, measuring less than 0.2 mm in thickness, manifested as linear artifacts in the coronal plane images (Figure 4). The most significant cause of increased length in the phantom was due to the error tolerance of the polyethylene stock. Each 1.59 mm segment had a maximum positive error tolerance of 0.889 mm. Assuming an average error tolerance (0.445 mm), the added length from stacking 62 segments is approximately 2.8 cm. Affine registration (shrinking the phantom volume in the anterior-posterior direction) was used to account for the difference in phantom and patient breast length during comparison of the coronal plane anatomy. To evaluate the phantom with rigid registration and avoid mathematically shrinking the image, the phantom must be machined from polyethylene stock with a tighter thickness error tolerance.

Since the design and construction of the phantom was based on high-resolution coronal bCT images, the phantom more accurately models the patient's breast in the coronal plane. The 2.8% difference between breast and phantom diameter may be due to a combination of inaccuracies in the segmentation and removal of the skin during image processing, machining of the breast segments, and application of the thermoplastic "skin". The similarity in coronal plane anatomy is exemplified by the strong coefficient of determination between line profiles through the registered volume data sets and the identical coronal plane anatomical noise power law exponent (β) for the patient's breast and the phantom. The values of β in the axial and sagittal planes differed between the phantom and the patient's breast, likely due to the artificial lengthening of the breast.

The water-jet cutting process resulted in a reduction of the outer adipose edge and expansion of the glandular tissue structure edges by approximately 0.1 mm. Adipose tissue segments surrounded by glandular tissue had to be excluded from the model as they would result in free-floating polyethylene pieces. As a result, the size of glandular tissue regions may be overestimated. Conversely, machining resolution limited the size of glandular tissue structures that could be included in the model, thus underestimating the total number of glandular tissue features. Overall, the volume glandular fraction of the phantom was less than that measured from the original patient images. Air bubbles were trapped in the glandular tissue compartment during phantom assembly, particularly near the nipple and chest wall; however, by using more sophisticated degassing techniques during phantom assembly, bubble trapping may be reduced. Since the phantom is constructed of polyethylene, it cannot be compressed and therefore cannot be studied using the geometry of mammography and DBT, but the modular nature does allow for the evaluation of individual thin breast segments.

Despite these limitations, the phantom developed in this study is the first to model the three-dimensional pendant breast and the underlying tissue distribution for a specific patient. The technique for phantom design and construction can be used to generate a patient-specific

breast phantom from any bCT data set and has been optimized for rapid production of subsequent phantoms. The two-compartment anthropomorphic phantom may allow for the evaluation of a variety of diagnostic and therapeutic modalities and provides a platform to perform measurements that may otherwise be difficult, unethical, or inappropriate to make *in vivo*.

Acknowledgments

The authors have no conflicts of interest to report. This work was funded in part by a grant from the National Institutes of Health (R01 EB002138).

References

Almberg SS, Lindmo T, Frengen J. Superficial doses in breast cancer radiotherapy using conventional and IMRT techniques: A film-based phantom study. Radiother Oncol. 2011

Bakic PR, Zhang C, Maidment ADA. Development and characterization of an anthropomorphic breast software phantom based upon region-growing algorithm. Medical Physics. 2011; 38:3165–76. [PubMed: 21815391]

Burgess AE, Jacobson FL, Judy PF. Human observer detection experiments with mammograms and power-law noise. Medical Physics. 2001; 28:419–37. [PubMed: 11339738]

Cai WX, Ning RL, Conover D. Scatter correction for clinical cone beam CT breast imaging based on breast phantom studies. J X-Ray Sci Technol. 2011; 19:91–109.

Caldwell CB, Yaffe MJ. Development of an Anthropomorphic Breast Phantom. Medical Physics. 1990; 17:273–80. [PubMed: 2333054]

Carton AK, Bakic P, Ullberg C, Derand H, Maidment AD. Development of a physical 3D anthropomorphic breast phantom. Med Phys. 2011; 38:891–6. [PubMed: 21452726]

Chen BY, Shorey J, Saunders RS, Richard S, Thompson J, Nolte LW, Samei E. An Anthropomorphic Breast Model for Breast Imaging Simulation and Optimization. Acad Radiol. 2011; 18:536–46. [PubMed: 21397528]

Chen L, Abbey CK, Nosrateih A, Lindfors KK, Boone JM. Anatomical complexity in breast parenchyma and its implications for optimal breast imaging strategies. Medical Physics. 2012; 39:1435–41. [PubMed: 22380376]

Darambara DG, Ma AKW, Gunn S. Introducing DeBRa: a detailed breast model for radiological studies. Phys Med Biol. 2009; 54:4533–45. [PubMed: 19556683]

Freed M, Badal A, Jennings RJ, de las Heras H, Myers KJ, Badano A. X-ray properties of an anthropomorphic breast phantom for MRI and x-ray imaging. Phys Med Biol. 2011a; 56:3513–33. [PubMed: 21606556]

Freed M, de Zwart JA, Loud JT, El Khouli RH, Myers KJ, Greene MH, Duyn JH, Badano A. An anthropomorphic phantom for quantitative evaluation of breast MRI. Medical Physics. 2011b; 38:743–53. [PubMed: 21452712]

Hammerstein GR, Miller DW, White DR, Masterson ME, Woodard HQ, Laughlin JS. Absorbed radiation dose in mammography. Radiology. 1979; 130:485–91. [PubMed: 760167]

Huang S-Y, Boone JM, Kai Y, Packard NJ, McKenney SE, Prionas ND, Lindfors KK, Yaffe MJ. The characterization of breast anatomical metrics using dedicated breast CT. Medical Physics. 2011; 38

Huang SY, Boone JM, Yang K, Kwan ALC, Packard NJ. The effect of skin thickness determined using breast CT on mammographic dosimetry. Medical Physics. 2008; 35:1199–206. [PubMed: 18491511]

Joensuu H, Lehtimaki T, Holli K, Elomaa L, Turpeenniemi-Hujanen T, Kataja V, Anttila A, Lundin M, Isola J, Lundin J. Risk for distant recurrence of breast cancer detected by mammography screening or other methods. JAMA. 2004; 292:1064–73. [PubMed: 15339900]

Lai CJ, Shaw CC, Chen LY, Altunbas MC, Liu XM, Han T, Wang TP, Yang WT, Whitman GJ, Tu SJ. Visibility of microcalcification in cone beam breast CT: Effects of x-ray tube voltage and radiation dose. Medical Physics. 2007; 34:2995–3004. [PubMed: 17822008]

Li CM, Segars WP, Tourassi GD, Boone JM, Dobbins JT. Methodology for generating a 3D computerized breast phantom from empirical data. Medical Physics. 2009; 36:3122–31. [PubMed: 19673211]

Lindfors KK, Boone JM, Nelson TR, Yang K, Kwan ALC, Miller DF. Dedicated breast CT: Initial clinical experience. Radiology. 2008; 246:725–33. [PubMed: 18195383]

Metheany KG, Abbey CK, Packard N, Boone JM. Characterizing anatomical variability in breast CT images. Medical Physics. 2008; 35:4685–94. [PubMed: 18975714]

Packard N, Boone JM. Glandular segmentation of cone beam breast CT volume images. Proc SPIE - Int Soc Opt Eng. 2007; 6510:651038.

Prionas ND, Huang S-Y, Boone JM. Experimentally determined spectral optimization for dedicated breast computed tomography. Medical Physics. 2011; 38:646–55. [PubMed: 21452702]

Shen Y, Yang Y, Inoue LY, Munsell MF, Miller AB, Berry DA. Role of detection method in predicting breast cancer survival: analysis of randomized screening trials. J Natl Cancer Inst. 2005; 97:1195–203. [PubMed: 16106024]

Shen Y, Yi Y, Zhong Y, Lai C-J, Liu X, You Z, Ge S, Wang T, Shaw CC. High resolution dual detector volume-of-interest cone beam breast CT----Demonstration with a bench top system. Medical Physics. 2011; 38:6429–42. [PubMed: 22149826]

Studholme C. RView. 2010

Yaffe MJ, Boone JM, Packard N, Alonzo-Proulx O, Huang SY, Peressotti CL, Al-Mayah A, Brock K. The myth of the 50–50 breast. Med Phys. 2009; 36:5437–43. [PubMed: 20095256]

Yang K, Kwan AL, Huang SY, Packard NJ, Boone JM. Noise power properties of a cone-beam CT system for breast cancer detection. Med Phys. 2008; 35:5317–27. [PubMed: 19175091]

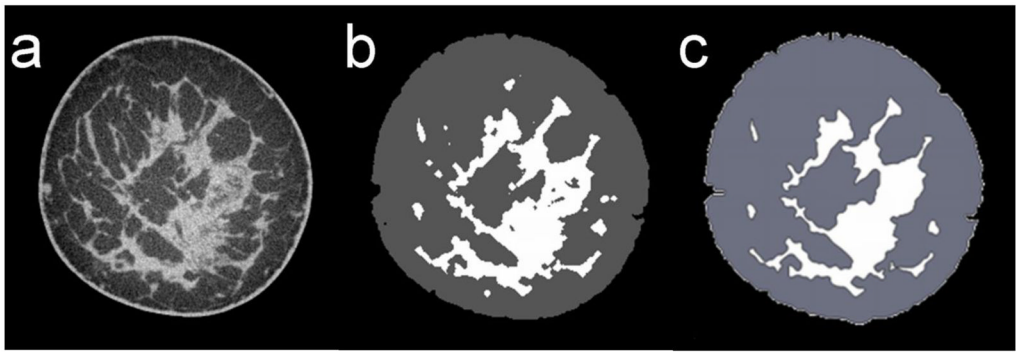

Figure 1.
Coronal patient images acquired on the dedicated bCT scanner (a) were smoothed and segmented (b) and used to generate a CAD model (c).

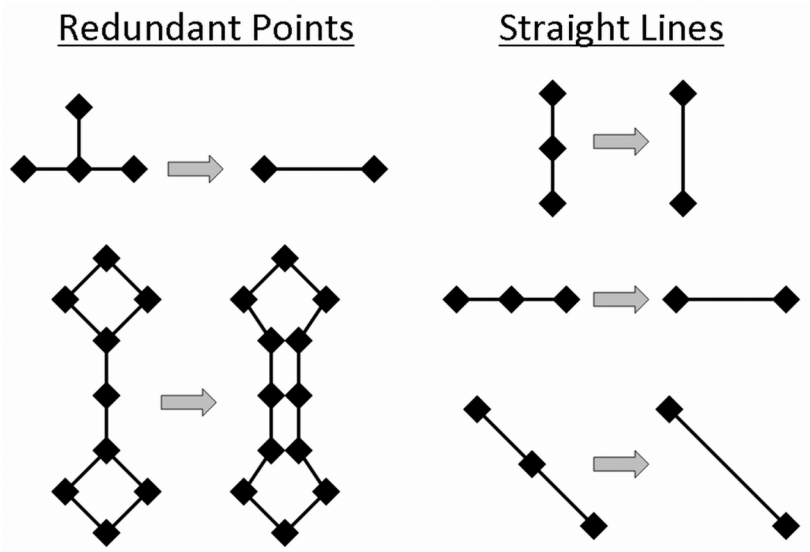

Figure 2.
The lists of points defining edges were post-processed to clarify redundancies and reduce the size of the data sets. Redundancies from single pixel protrusions were removed and those from single pixel-wide septa connecting open loops were expanded. Straight lines were simplified to their start and end points.

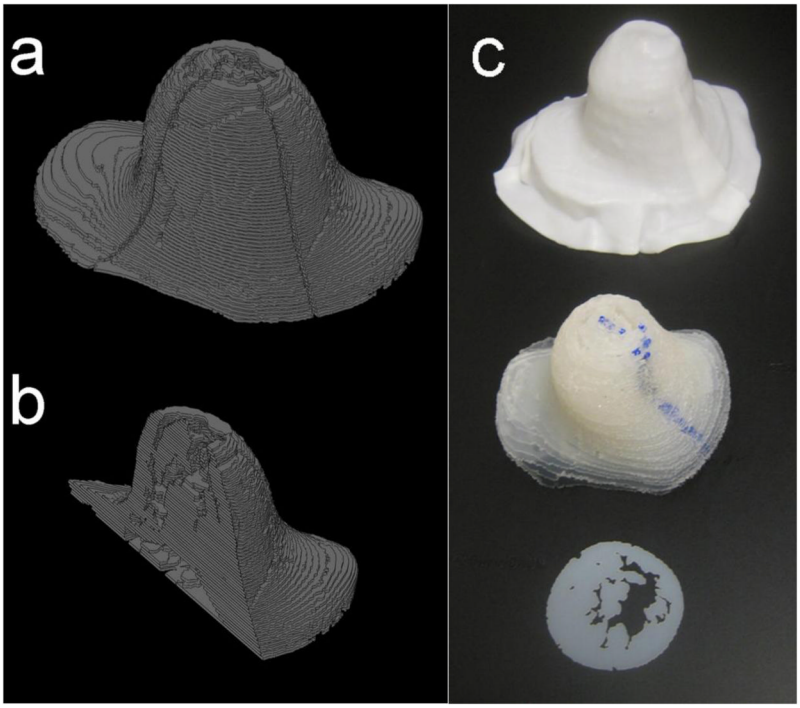

Figure 3.
CAD model of the entire phantom (a) and a cross-section through the phantom (b) along with a physical image showing the thermoplastic “skin”, stacked polyethylene breast segments, and a single breast segment of the two-compartment anthropomorphic phantom (c).

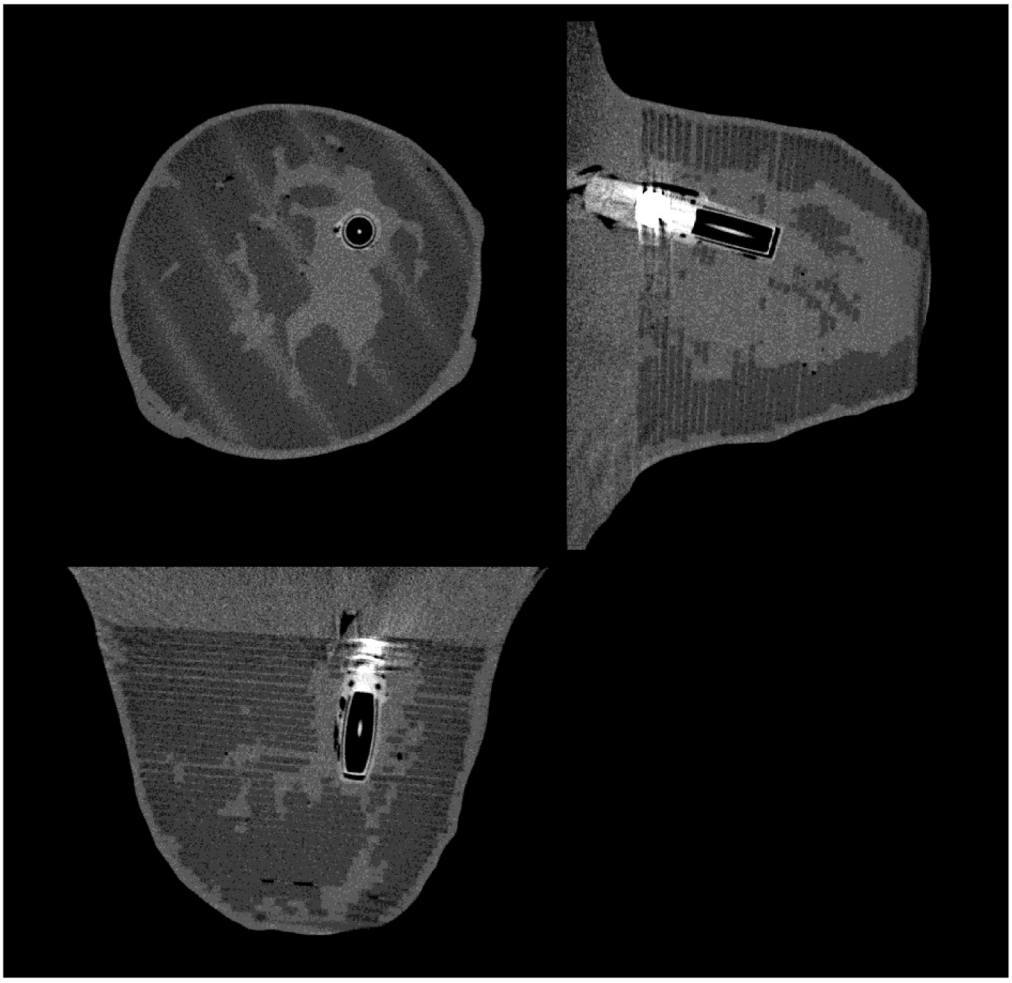

Figure 4.
Breast CT image of the phantom with a thimble real-time air ionization chamber positioned in the mid-breast region.

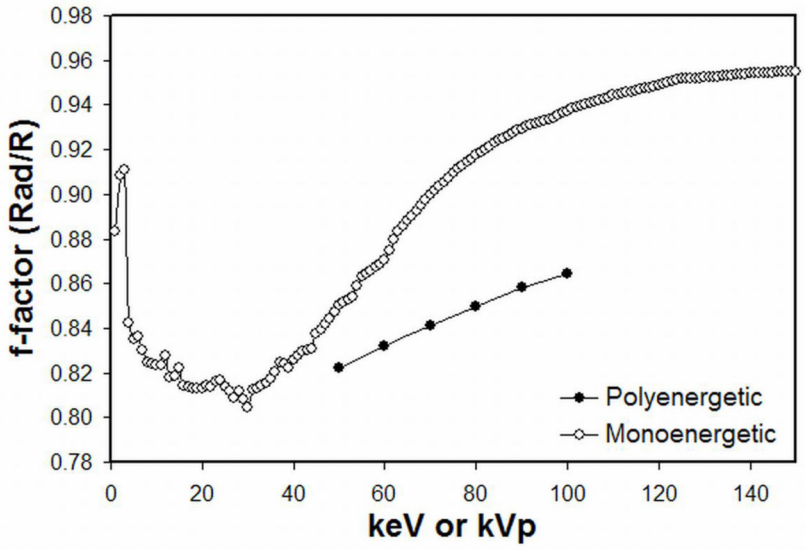

Figure 5.

Roentgen to Rad conversion factors (f-factor) were used to calculate dose deposited to glandular tissue. The polyenergetic f-factors for the spectra evaluated in the study and the monoenergetic f-factor values used to derive them are plotted.

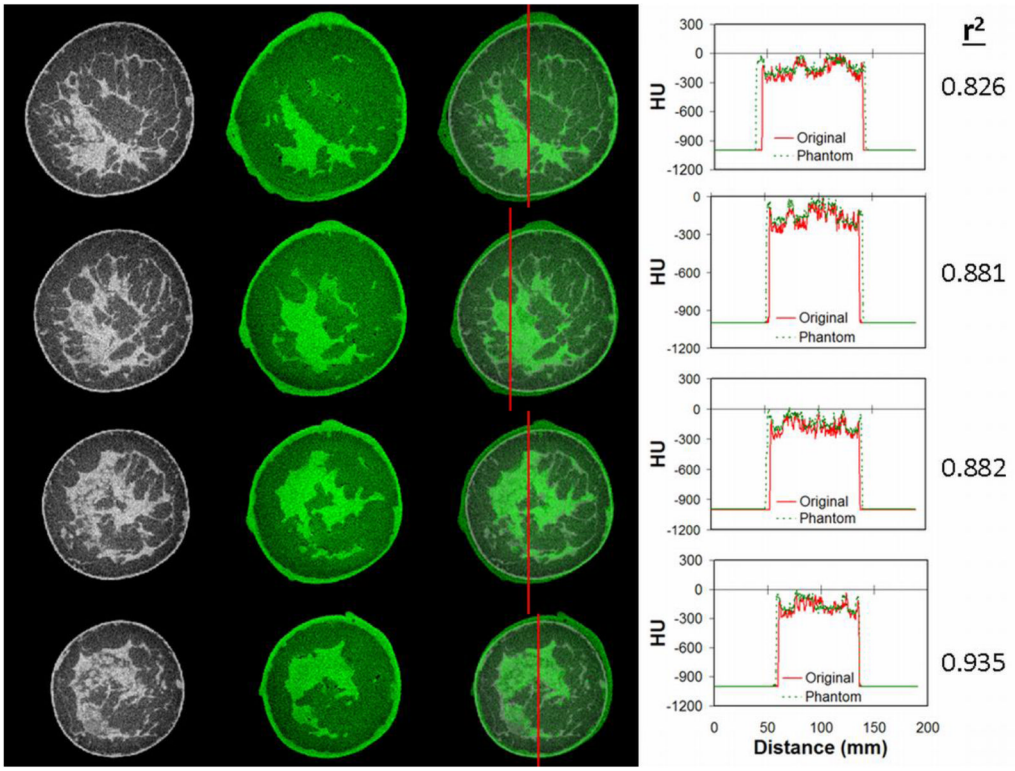

Figure 6.

Four representative coronal breast images from the original patient bCT image set (first column) and the corresponding segments from a bCT scan of the phantom (second column) showed similar tissue distributions (overlay shown in third column). Line profiles through the registered volume data sets (fourth column) demonstrated agreement in the gray scale profile, as quantified using the coefficient of determination (r^2). The rows, from top to bottom, correspond to breast segments 2.8, 3.9, 4.8, and 5.6 cm from the chest wall, respectively.

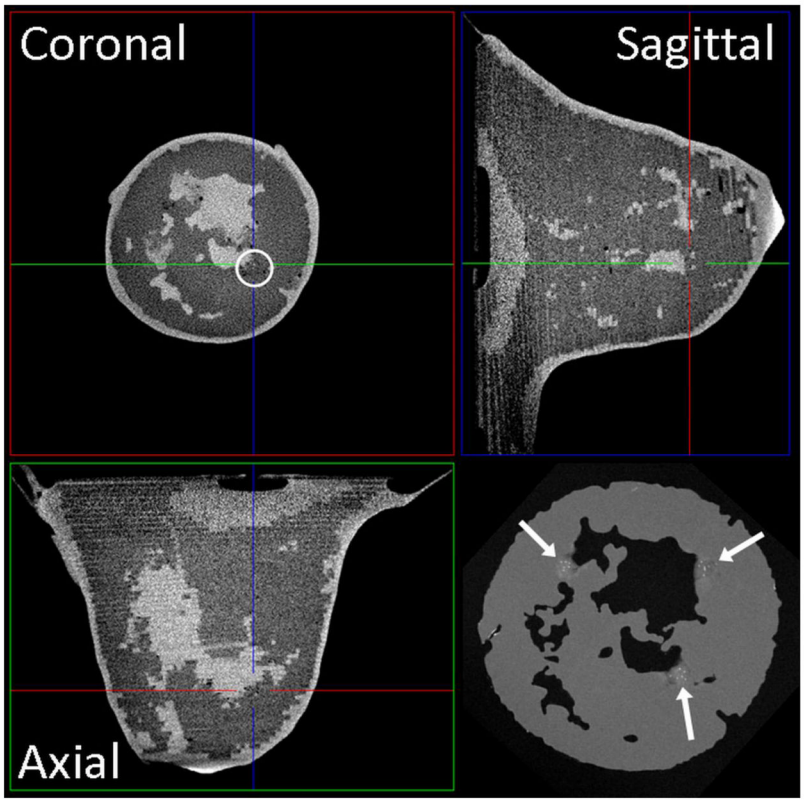

Figure 7.
Three clusters of microcalcifications (arrows) were embedded into a segment of the breast phantom, as shown in the mammographic projection image of the breast segment (lower right). Orthogonal bCT images demonstrate visualization of the microcalcification cluster at the 4 o'clock position (circled), particularly in the coronal image (upper left). Microcalcifications were also present in adjacent CT slices.

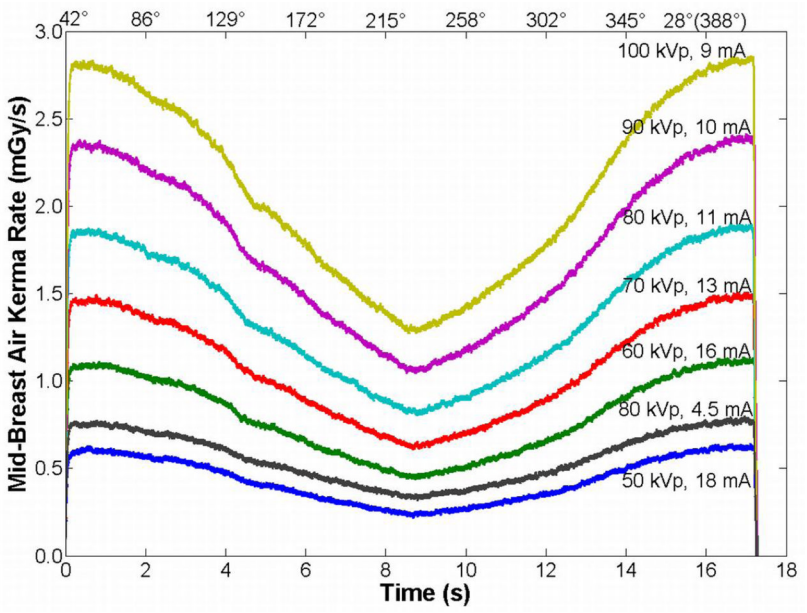

Figure 8.

Dosimetry using the phantom was demonstrated by measuring real-time air kerma rate within the breast phantom during a bCT scan for various different technique factors. The x-axis is given as time during the scan along the bottom and angular position of the source along the top, where 0°(360°) is defined as the superior aspect of the breast. The maximum and minimum air kerma rates occurred when the x-ray source was closest and farthest from the dosimeter, respectively.

Table 1

The breast phantom was scanned using the listed technique factors. Air kerma was measured in air and in the breast phantom in order to calculate the mean glandular dose (MGD) and mid-breast point dose in the glandular tissue compartment, respectively. Half-value layer (HVL) is given for each technique.

kVp	mA	HVL (mm Al)	Air kerma rate in air (mGy/min)	Air kerma rate in phantom (mGy/min)	MGD (mGy)	Point dose (mGy)	% Difference
50	18	3.11	36.1	26.1	6.5	7.0	8.2
60	16	3.85	59.9	47.7	12.0	13.0	7.5
70	13	4.50	76.3	64.3	16.5	17.7	6.5
80	4.5	5.06	38.4	33.7	8.7	9.4	7.4
80	11	5.06	93.7	82.2	21.3	22.8	7.1
90	10	5.76	116.7	105.1	27.6	29.5	6.6
100	9	6.29	137.2	125.9	33.3	35.6	6.7
						Average	7.1
						Std. Dev.	0.6

Phys Med Biol. Author manuscript; available in PMC 2013 July 07.